Triangular Grids: A Review of Resonator and Waveguide Analysis with Classical FIT and Some Reflections on Yee-like FIT- and FEM-Schemes

URSULA VAN RIENEN
Institute of General Electrical Engineering
Rostock University
D-18051 Rostock, Germany
ursula.van-rienen@etechnik.uni-rostock.de

***Abstract*— The focus of this paper is on the solution of Maxwell's equations on triangular orthogonal grids for time-harmonic fields in cylindrically symmetric resonators and general time dependant fields in length-homogeneous waveguides, respectively. The method is based on the Finite Integration Technique (FIT) [1], [2]. The 2D simulation on a structured triangular grid combines the advantages of FIT, as e.g. the consistency of the method or the numerical advantage of banded system matrices, with the geometrical flexibility of non-coordinate grids. FIT on triangular grids was first introduced in [3], [4][1]. This paper presents a review describing the underlying theory in FIT operator notation first introduced in [2] and puts this classical approach for FIT on triangular grids in relation to actual research in the field.**

I. CLASSICAL FINITE INTEGRATION TECHNIQUE ON A STRUCTURED TRIANGULAR GRID

The Finite Integration Technique solves Maxwell's equations on a pair of dual grids. Actual implementations generally work on a rectangular two- or three-dimensional domain Ω. Sometimes the field-carrying domain Ω_s is only a sub-domain of the domain Ω: $\Omega = \Omega_s \cup \Omega_o$. The solution domain might be composed of several subregions: $\Omega_s = \cup_i \Omega_{s_i}$. Discretization on Ω rather than on Ω_s has the advantage of allowing for higher topological regularity leading to matrices with regular (band) pattern. Usually Ω_o, the overhead, is relatively small.

FIT yields an *exact* representation of Maxwell's equations in integral form on a grid duplet $(G, \widetilde{G})$, denoted as *Maxwell-Grid-Equations*:

$$\begin{aligned} \mathbf{C}\widehat{\mathbf{e}} &= -\tfrac{\partial}{\partial t}\widehat{\widetilde{\mathbf{b}}}, & \mathbf{S}\widehat{\widetilde{\mathbf{b}}} &= \mathbf{0}, \\ \widetilde{\mathbf{C}}\widehat{\mathbf{h}} &= \tfrac{\partial}{\partial t}\widehat{\widetilde{\mathbf{d}}} + \widehat{\widetilde{\mathbf{j}}}, & \widetilde{\mathbf{S}}\widehat{\widetilde{\mathbf{d}}} &= \mathbf{q}. \end{aligned} \tag{1}$$

The linear operators $\mathbf{C}, \widetilde{\mathbf{C}}, \mathbf{S}$ and $\widetilde{\mathbf{S}}$, the so-called grid voltages $\widehat{\mathbf{e}}$ and $\widehat{\mathbf{h}}$ as well as the grid fluxes $\widehat{\widetilde{\mathbf{b}}}, \widehat{\widetilde{\mathbf{d}}}$ and $\widehat{\widetilde{\mathbf{j}}}$ and the charge vector $\mathbf{q}$ will be introduced below.

Talking of an *exact* representation relates to the discretization error. The topic of errors is treated in more detail in the next subsection.

[1]URMEL–T is the resonator and waveguide code based on the classical FIT on triangular grids described here.

The FIT grid duplet $(G, \widetilde{G})$ is not necessarily coordinate-bounded, not necessarily orthogonal, not necessarily regular. Often the solution domain Ω_s possesses symmetries or some geometrical invariance such that the 3D problem may be reduced to a 2D problem by appropriate variable separation. For example, this is the case for cylindrically symmetric resonators and longitudinally invariant waveguides as treated in this paper.

The linear operators $\mathbf{C}$, $\widetilde{\mathbf{C}}$, $\mathbf{S}$ and $\widetilde{\mathbf{S}}$ in (1) can be interpreted as discrete curl operators $\mathbf{C}, \widetilde{\mathbf{C}}$, discrete divergence $\mathbf{S}, \widetilde{\mathbf{S}}$ and discrete gradient operators $\mathbf{G} = -\widetilde{\mathbf{S}}^T, \widetilde{\mathbf{G}} = -\mathbf{S}^T$. The discrete operators fulfill the following key properties

$$\mathbf{C} = \widetilde{\mathbf{C}}^T, \tag{2}$$

$$\mathbf{S}\,\mathbf{C} = \widetilde{\mathbf{S}}\,\widetilde{\mathbf{C}} = \mathbf{0}, \tag{3}$$

as generally shown in [2]. These equations, especially that the transpose $\widetilde{\mathbf{C}}^T$ of the dual curl operator equals the primary curl operator $\mathbf{C}$, represent a topological property resulting from the duality of the grids. For further analytical and algebraic properties resulting from these basic equations the reader is referred e.g. to [2], [5] and [6]. Conservation of energy is just one of the continuous laws for which a proof can be given for the discrete FIT equations, too.

The vectors $\widehat{\mathbf{e}}, \widehat{\mathbf{h}}$, etc. hold scalar state variables defined as field integrals along edges $L_i, \tilde{L}_i$ and across facets $A_i, \tilde{A}_i$, yielding the so-called *grid voltages* $\widehat{\mathbf{e}}, \widehat{\mathbf{h}}$ and *grid fluxes* $\widehat{\widetilde{\mathbf{b}}}, \widehat{\widetilde{\mathbf{d}}}, \widehat{\widetilde{\mathbf{j}}}$ on the primary grid G and the dual grid $\widetilde{G}$, respectively:

$$\begin{aligned} \widehat{e}_i &= \int_{L_i} \boldsymbol{E}\cdot d\boldsymbol{s}, & \widehat{\tilde{b}}_i &= \int_{A_i} \boldsymbol{B}\cdot d\boldsymbol{A}, \\ \widehat{h}_i &= \int_{\tilde{L}_i} \boldsymbol{H}\cdot d\boldsymbol{s}, & \widehat{\tilde{d}}_i &= \int_{\tilde{A}_i} \boldsymbol{D}\cdot d\boldsymbol{A}, \\ & & \widehat{\tilde{j}}_i &= \int_{\tilde{A}_i} \boldsymbol{J}\cdot d\boldsymbol{A}. \end{aligned} \tag{4}$$

The vector $\mathbf{q}$ holds discrete grid charges q_i which are allocated in the points (nodes) of the primary grid G and are defined as a volume integral over the space charge ρ contained in the surrounding dual grid volume $\tilde{V}_i$:

$$q_i = \int_{\tilde{V}_i} \rho dV. \tag{5}$$

With these definitions it is straightforward to derive the discrete form of Maxwell's equations for a given FIT grid duplet $(G, \widetilde{G})$. It will be shown for a 2D triangular grid G with hexagonal dual grid $\widetilde{G}$ in subsection I-A.

The choice of a specific grid is mainly influenced by the following aspects which have to be balanced well:

1) a good approximation of the boundary $\partial\Omega_s$ with as few grid points as possible in order to decrease the spatial discretization error while keeping memory requirements as small as possible,
2) a most regular grid in order to decrease the condition of the resulting linear or eigenvalue systems yielding a smaller iterative convergence error and/or faster convergence speed,
3) a fast and robust grid generation for arbitrary domains Ω_s, especially those with $\Omega_s = \cup_i \Omega_{s_i}$.

There are many more aspects influencing the solution quality which are out of the focus of this paper which concentrates on some basic issues.

Among several types of grids on which FIT has been implemented until today there were first a 2D [1] and later a 3D [2] Cartesian grid allowing for diagonal filling in order to avoid the 'staircase' approximation still usual in FDTD. This grid is easy to implement but good convergence can not always be reached depending on the specific boundary shape of $\partial\Omega_s$. This gave reason to implement FIT on the regular triangular grid [3] described in this paper which achieves good boundary approximations with rather few grid points. Other examples are the non-orthogonal second order convergent quadrangular 3D grid described in [6] and the so-called Conformal FIT (briefly CFIT) [7], on Cartesian grids, also being second order accurate but numerically less expensive. All of these specific grids have their pro's and con's regarding the aspects described above.

A. *The Triangular Grid and its Dual Grid*

In the following, we describe an application of FIT on a structured 2D triangular grid. The method has been implemented in the URMEL-T code [3]. This may be used for longitudinal and transversal eigenmode computation in cylindrically symmetric resonators and for studies of waves excited in longitudinally invariant waveguides. Often, this 2D code is used in design studies in combination with a 3D code, see e.g. [8]. Also, 2D computations may be used for the simulation of the rf properties of cylindrically symmetric subsections of complex structures when methods using the scattering matrix formulations are applied, see e.g. [9] or [10].

Without loss of generality it is assumed that the electric voltages are allocated on the triangular grid G and the magnetic voltages on the dual grid $\tilde{G}$ (see [4] for special details on the alternative allocation). The mesh generator starts off with a regular triangulation for Ω which is as close as possible to an equilateral triangulation (cf. Fig 3 in subsection III-A). Then, grid points are moved onto the boundary $\partial\Omega_s$ resp. boundaries $\partial\Omega_{s_i}$ for $\Omega_s = \cup_i \Omega_{s_i}$, i.e. for solution domains which consist out of several subregions Ω_{s_i}. Finally the triangulation of Ω is equilibrated.

For the equilibration all grid points are taken as mass points and all edges as springs. Then, the goal is to find an equilibrium, i.e. to minimize the potential which corresponds to the distance squared. The elastic force of a spring is given by Hooke's law $\mathbf{F} = -k\mathbf{r}$ where $\mathbf{r}$ is the displacement from equilibrium $\mathbf{r} = 0$ and k is the spring constant. The potential energy of motion on a straight line through $\mathbf{r} = 0$ is given by

$$E_{pot}(s) = \frac{1}{2} k s^2 \tag{6}$$

where s corresponds to the distance of two grid points and k is chosen to $k = 1$ for all points. Points on the boundaries $\partial\Omega$ of the mesh and $\partial\Omega_s$ or $\partial\Omega_{s_i}$, respectively, of the solution domain(s) need a special treatment. The coordinates can be treated one after the other. For each coordinate, a sparse linear system of equations results from (6) and is solved iteratively. Remaining obtuse triangles are searched for. In some typical cases they can be individually transformed into acute triangles, too. Details on this algorithm may be found in [13].

Optimally, the mesh generator can set up the completely orthogonal dual grid $\tilde{G}_\perp$ composed of the perpendicular bisectors of the elementary lines L_i. The intersections of the perpendicular bisectors, the circumcenters, give the dual grid points $\tilde{P}_i$. Its elementary areas $\tilde{A}_i$ in the grid plane are general hexagons, cf. Fig. 1. In the construction of the material operators also areas normal to the (x, y)-grid plane are needed thus a *virtual* mesh extends for $\pm\Delta z/2$ in the longitudinal z-direction for the waveguide case as displayed in Fig. 2 and for $\pm\Delta\varphi/2$ in the azimuthal φ-direction for the resonator case, respectively.

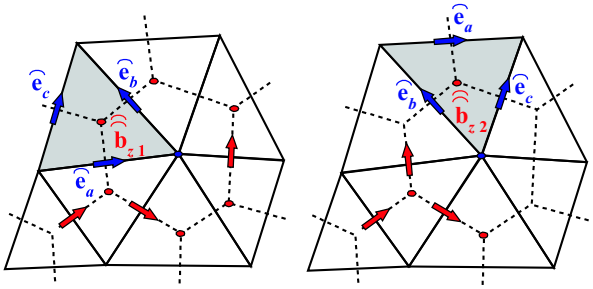

Fig. 1. Classical triangular FIT grid with its dual (hexagonal) grid, and some of the electric and magnetic state variables. The two kinds of primary cells (vertex up and vertex down) associated to each grid point are highlighted each. (This illustration refers to the waveguide case, i.e. (x, y, z)-coordinates. For the resonator case, i.e. (r, φ, z)-coordinates, $\widehat{\widehat{b}}_{z1}$ and $\widehat{\widehat{b}}_{z2}$ just have to be replaced by $\widehat{\widehat{b}}_{\varphi 1}$ and $\widehat{\widehat{b}}_{\varphi 2}$, respectively)

$\tilde{G}_\perp$ is a Delaunay-Voronoi mesh for the complete domain Ω. For this dual-orthogonal FIT grid the continuity of tangential electric field and normal magnetic flux is preserved on all inner boundaries $\partial\Omega_{s_i}$ of different materials within Ω_s.

Only if all triangles of the grid G inside Ω_s are acute or right-angled all grid points $\tilde{P}_i$ of the dual grid $\widetilde{G}_\perp$ lie inside

the i-th triangle. It may well happen that obtuse triangles occur near the boundary of Ω_s some of which remain after equilibration of the grid. In that case the circumcenters are chosen for $\tilde{P}_i$ in all acute triangles and barycenters in the (usually very few, cf. subsection III-C) obtuse triangles. Then, the approximation order p is locally reduced to first order, overall p typically still has a value close (but smaller than) two as described below.

B. The Grid Operators on the Triangular Grid

In the previous section the *Maxwell-Grid-Equations* (1) were generally defined. Now we will deal with some of the grid operators on the triangular grid. Special interest is laid on the material operators.

*1) **The curl- and divergence operators**:* As an example for the derivation of the Maxwell-Grid-Equations on the orthogonal triangular grid we will first regard Faraday's law. With the notations as in Fig. 1 we get:

$$\widehat{e}_a + \widehat{e}_b - \widehat{e}_c = -\frac{\partial}{\partial t}\widehat{\widehat{b}}_{z1}, \tag{7}$$

$$-\widehat{e}_a - \widehat{e}_b + \widehat{e}_c = -\frac{\partial}{\partial t}\widehat{\widehat{b}}_{z2}. \tag{8}$$

Since there are only grid voltages and fluxes, the time derivative and a linear combination with factors ± 1 this is an *exact* representation of Faraday's law on the primary cell, i.e. the discretization error is zero per definitionem.

Collecting all voltages and fluxes in the vectors $\widehat{\mathbf{e}}$ and $\widehat{\widehat{\mathbf{b}}}$ and the incidences in the matrix $\mathbf{C}$ yields Faraday's equation on the grid as presented in (1).

Integration of Coulomb's law takes place over the surface of a prism the base of which is indicated by the dotted line in Fig. 1. One of its side faces is depicted in Fig. 2. The flux $\widehat{\widehat{d}}_z$ is allocated in the middle of the hexagonal's base while $\widehat{\widehat{d}}_{z_{\mathrm{back}}}$ and $\widehat{\widehat{d}}_{z_{\mathrm{front}}}$ lie $\pm\Delta z/2$ apart in the virtual grid in z-direction and may be determined from $\widehat{\widehat{d}}_z$ via (17). Then, for Coulomb's law we get:

$$\begin{aligned} &-\widehat{\widehat{d}}_{a_{\mathrm{left}}} + \widehat{\widehat{d}}_{a_{\mathrm{right}}} - \widehat{\widehat{d}}_{b_{\mathrm{bottom}}} + \widehat{\widehat{d}}_{b_{\mathrm{top}}} \\ &-\widehat{\widehat{d}}_{c_{\mathrm{bottom}}} + \widehat{\widehat{d}}_{c_{\mathrm{top}}} - \widehat{\widehat{d}}_{z_{\mathrm{back}}} + \widehat{\widehat{d}}_{z_{\mathrm{front}}} = q. \end{aligned} \tag{9}$$

The fluxes are collected in the vector $\widehat{\widehat{\mathbf{d}}}$, charges in a vector $\mathbf{q}$ and the incidences in the matrix $\widetilde{\mathbf{S}}$ yielding Coulomb's law as presented in (1).

The set-up of $\widetilde{\mathbf{C}}$ and $\mathbf{S}$ is done analogously just on the other grid, each. The discrete curl operators $\mathbf{C}$ and $\widetilde{\mathbf{C}}$ and the discrete divergence operators $\mathbf{S}$ and $\widetilde{\mathbf{S}}$ obviously reflect the topology of the triangular (primary) grid, its dual hexagonal grid and the enumeration. See [11] for more details.

*2) **The material operators**:* In order to derive a discrete equivalent of the constitutive laws we need to find a linear map between grid voltages and fluxes:

$$\widehat{\widehat{\mathbf{d}}} = \mathbf{M}_\epsilon \widehat{\mathbf{e}}, \qquad \widehat{\widehat{\mathbf{b}}} = \mathbf{M}_\mu \widehat{\mathbf{h}}, \qquad \widehat{\widehat{\mathbf{j}}} = \mathbf{M}_\sigma \widehat{\mathbf{e}}. \tag{10}$$

In Ω_s we assume loss free material, i.e. ϵ, μ and σ are real. Here the conductivity is assumed to be equal to zero (except for the perfect conductor material).

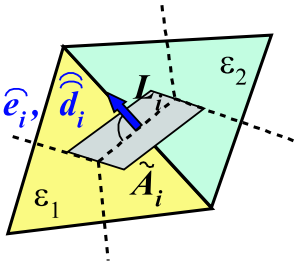

Fig. 2. Classical triangular FIT grid with its dual (hexagonal) grid: Zoom to some dual grid area $\tilde{A}_i$ normal to primary grid plane. The area $\tilde{A}_i$ and the path length L_i are used for material averaging.

In classical FIT, the *material operators* $\mathbf{M}_\epsilon, \mathbf{M}_\mu$ and $\mathbf{M}_\sigma$ are determined by local averaging of material quantities. This is motivated as follows: Let us regard the dual grid area $\tilde{A}_i$ depicted in Fig. 2. The primary edge L_i perpendicularly intersects $\tilde{A}_i$. The electric voltage $\widehat{e}_i$ along the edge and the electric flux $\widehat{\widehat{d}}_i$ through the area are defined as in (4). They are collinear. We may approximate both integrals with help of some *virtual* constant mean value $\mathrm{e_i}$. For $\widehat{e}_i$, we directly get

$$\begin{aligned} \widehat{e}_i &= \int_{L_i} \boldsymbol{E}(\boldsymbol{r}) \cdot d\boldsymbol{s} \\ &= (\mathrm{e_i} + O({L_i}^m)) \int_{L_i} ds \\ &= \mathrm{e_i} \cdot L_i + O({L_i}^m). \end{aligned} \tag{11}$$

Obviously, this is the moment when the introduction of some discretization error gets unavoidable. The local approximation order m is $m = 2$ if $\mathrm{e_i}$ is exactly allocated in the middle point of L_i.

In order to get a similar expression for $\widehat{\widehat{d}}_i$ we have to deal with the fact that the dual area $\tilde{A}_i$ intersects several triangles, i.e. primary cells, which all may be filled with different material. For the topological regular grid treated here we have the case shown in Fig. 2 where two cells are intersecting and secondly that one of six intersected triangles indicated by the dotted lines in Fig. 1. So, we introduce an effective permittivity

$$\epsilon_{\mathrm{eff},i} = \frac{1}{\tilde{A}_i} \int_{\tilde{A}_i} \epsilon(\boldsymbol{r})\, dA. \tag{12}$$

Then, we receive the following expression for $\widehat{\widehat{d}}_i$

$$\begin{aligned} \widehat{\widehat{d}}_i &= \int_{\tilde{A}_i} \boldsymbol{D}(\boldsymbol{r}) \cdot d\boldsymbol{A} = \int_{\tilde{A}_i} \epsilon(\boldsymbol{r})\, \boldsymbol{E}(\boldsymbol{r}) \cdot d\boldsymbol{A} \\ &= \left(\mathrm{e_i} + O(\tilde{A}_i^n)\right) \int_{\tilde{A}_i} \epsilon(\boldsymbol{r})\, dA \\ &= \epsilon_{\mathrm{eff},i} \cdot \mathrm{e_i} \cdot \tilde{A}_i + O(\tilde{A}_i^n). \end{aligned} \tag{13}$$

For equal ϵ in all intersected primary cells the local approximation order n would be $n = 4$ if $\tilde{A}_i$ would be a square and $\mathrm{e_i}$ would be exactly allocated in its middle.

We are searching for the entry $M_{\epsilon,i}$ connecting $\widehat{e}_i$ and $\widehat{\tilde{d}}_i$ in the constitutive law $\widehat{\tilde{\mathbf{d}}} = \mathbf{M}_\epsilon \widehat{\mathbf{e}}$. Since, by orthogonality, we have the one-to-one relation between $\widehat{e}_i$ and $\widehat{\tilde{d}}_i$ they are just connected via multiplication by the diagonal entry $M_{\epsilon,i}$ of the operator $\mathbf{M}_\epsilon$ which is purely diagonal. Thus we regard the quotient of $\widehat{e}_i$ and $\widehat{\tilde{d}}_i$ in order to derive an expression for the $i-$th diagonal entry of the material operator $\mathbf{M}_\epsilon$. From (11) and (13) we get

$$\frac{\widehat{\tilde{d}}_i}{\widehat{e}_i} = \frac{\int_{\tilde{A}_i} \epsilon(\boldsymbol{r}) \boldsymbol{E}(\boldsymbol{r}) \cdot d\boldsymbol{A}}{\int_{L_i} \boldsymbol{E}(\boldsymbol{r}) \cdot d\boldsymbol{s}} = \frac{\epsilon_{\text{eff},i} \cdot \tilde{A}_i}{L_i} + O(L^p). \qquad (14)$$

Thus the local discretization error is linear to quadratic. It depends on the degree of regularity in the mesh: For an equidistant Cartesian mesh the error is quadratic.

We can proceed similarly for the constitutive law connecting the magnetic voltage $\widehat{\tilde{h}}_i$ along a dual edge $\tilde{L}_i$ and the magnetic flux $\widehat{\tilde{b}}_i$ through the corresponding primary area A_i (cf. e.g. [12] for more details). Then, the entries of the permittivity and permeability operator are set to

$$M_{\epsilon,i} = \frac{\epsilon_{\text{eff},i} \cdot \tilde{A}_i}{L_i}, \qquad M_{\mu,i} = \frac{\mu^{-1}_{\text{eff},i} \cdot \tilde{L}_i}{A_i}. \qquad (15)$$

Thus, the construction of $\mathbf{M}_\epsilon$ is based on area-wise averaging (cf. Fig. 2) and the construction of $\mathbf{M}_\mu$ is based on lengthwise averaging. The conductivity operator $\mathbf{M}_\sigma$ is defined in full analogy to $\mathbf{M}_\epsilon$. These operators are diagonal and have only positive entries. This is of special importance for time domain simulations (cf. subsection II-A).

In classical FIT on *orthogonal* grids the transfer of the electromagnetic material equations to the grid space generally results with *diagonal* material operators $\mathbf{M}_\epsilon, \mathbf{M}_\mu, \mathbf{M}_\sigma$.

C. *Cylindrically Symmetric Resonators and Length-Homogeneous Waveguides*

As described in [3], [4], classical FIT on triangular grids was implemented to solve for eigenmodes in cylindrically symmetric resonant cavities and for fields in translational waveguides. If Ω_s is longitudinally invariant a variable separation is possible for the longitudinal coordinate:

$$\boldsymbol{E}(x, y, z) = \boldsymbol{E}_0(x, y) e^{i\beta z} \qquad (16)$$

with the propagation constant β. On the discrete level this can be written as

$$\boldsymbol{E}(x, y, \Delta z) = \boldsymbol{E}_0(x, y) e^{i\beta\Delta z} \doteq \boldsymbol{E}_0(x, y)(1 + i\beta\Delta z) \quad (17)$$

with some *virtual* step size Δz in the third dimension of space which is only needed 'on paper' to set up the discrete equations like (9) or (13).

Furthermore, it is assumed that the fields are time-harmonic such that a description by a Fourier series is possible. Finally, the materials are assumed loss free, and non-conducting.

So, additionally normalizing with the root of the wave impedance $Z_0 = \sqrt{\mu_0/\epsilon_0}$ and the admittance $Y_0 = \sqrt{\epsilon_0/\mu_0}$, respectively, where ϵ_0 and μ_0 are the permittivity and permeability of vacuum, we may write

$$\boldsymbol{E} = \sqrt{Z_0} \sin \omega t \boldsymbol{E}', \qquad \boldsymbol{H} = \sqrt{Y_0} \cos \omega t \boldsymbol{H}' \qquad (18)$$

with the normalized fields $\boldsymbol{E}'$ and $\boldsymbol{H}'$. Maxwell's equations are then discretized with FIT using the normalized fields as given in (18).

In the resonator case the variable separation is done for the azimuthal coordinate φ and the normalized fields $\boldsymbol{E}'$ and $\boldsymbol{H}'$ can then be written as

$$\begin{aligned} \boldsymbol{E}'(r, \varphi, z) &= \sum_{m=0}^{\infty} [\, E'_{m,r}(r, z) \cos m\varphi \, \boldsymbol{e}_r \\ &\quad + E'_{m,\varphi}(r, z) \sin m\varphi \, \boldsymbol{e}_\varphi \\ &\quad + E'_{m,z}(r, z) \cos m\varphi \, \boldsymbol{e}_z \,], \\ \boldsymbol{H}'(r, \varphi, z) &= \sum_{m=0}^{\infty} [\, H'_{m,r}(r, z) \sin m\varphi \, \boldsymbol{e}_r \\ &\quad + H'_{m,\varphi}(r, z) \cos m\varphi \, \boldsymbol{e}_\varphi \\ &\quad + H'_{m,z}(r, z) \sin m\varphi \, \boldsymbol{e}_z \,] \end{aligned} \qquad (19)$$

expressing the periodicity with period 2π in the azimuthal variable φ. Then Maxwell's equations are solved for each azimuthal mode number m separately. In case of time harmonic fields the divergence equation is *automatically* fulfilled as was shown in [1]. Therefore it is possible to resolve the equation $\widetilde{\mathbf{S}}\widehat{\tilde{\mathbf{d}}} = 0$ for the azimuthal flux density $\widehat{\tilde{d}}_\varphi$ and substitute $\widehat{\tilde{d}}_\varphi$ resp. $\widehat{e}_\varphi$ in the remaining field equations. This formulation reduces the dimension of the system to be solved by the number of grid points N.

Finally, a linear algebraic eigenvalue problem results. In the waveguide case it has the squared propagation constants β^2 for a given frequency ω as eigenvalues, in the resonator case the eigenmodes are just the eigenfrequencies of the resonant monopole ($m = 0$), dipole ($m = 1$) and higher order modes. The propagation constant β may also take complex values, i.e. all waves including complex modes are found for waveguides. More details on these equations and on URMEL-T may be found in [4] and [11] or [13]. Some examples will be given in section III below.

II. Considerations on FIT and FEM with Whitney Forms, FEM on Orthogonal Grids and Time Domain Simulations

In recent years there have been intensive studies on different approaches more or less related to the classical FIT on triangular grids. In this section, we will try to summarize some of the results and discuss some aspects which are important if triangular grids shall be used for time domain simulations. Of course, this can only touch a few of the wide variety of recent time-domain approaches with FEM, see [14] and references therein.

A. *Important Aspects for Time Domain Simulation*

The stability of any time domain scheme, either FEM or FIT, is determined by the characteristics of its material operators. In [15] it was shown that positive definiteness of the material matrices is a sufficient condition for energy

conservation and stability in Yee's leap-frog-scheme [16]. Any scheme with *diagonal* material operators, having only positive entries ensures this condition.

The second advantage of diagonal material operators is the possibility to directly invert these matrices and thus to set-up an explicit iteration scheme which is of great advantage with regard to the numerical effort compared to implicit schemes. Thus it is a key point for the construction of a stable explicit time domain simulation to use a discretization scheme with diagonal material operators. Classical FIT on orthogonal grids fulfills these conditions.

Using Yee's leap-frog-scheme with FIT the equations for $\widehat{\mathbf{e}}$ and $\widehat{\mathbf{b}}$ are generally given as (cf. [15] or [12])

$$\widehat{\mathbf{b}}^{k+1} = \widehat{\mathbf{b}}^{k} - \Delta t\, \mathbf{C}\, \widehat{\mathbf{e}}^{k+\frac{1}{2}}, \tag{20}$$

$$\widehat{\mathbf{e}}^{k+\frac{3}{2}} = \widehat{\mathbf{e}}^{k+\frac{1}{2}} + \Delta t\, \mathbf{M}_{\epsilon}^{-1}(\widetilde{\mathbf{C}}\mathbf{M}_{\mu}^{-1}\widehat{\mathbf{b}}^{k+1} - \widehat{\mathbf{j}}^{k+1}). \tag{21}$$

Here $\widehat{\mathbf{b}}^{k+1}$ denotes $\widehat{\mathbf{b}}$ at time $t = t_0 + k\Delta t$ while $\widehat{\mathbf{e}}^{k+\frac{1}{2}}$ is allocated at time $t = t_0 + (k+\frac{1}{2})\Delta t$. The main idea of Yee's scheme is to use a staggered grid in time domain, too. For the time derivatives, central difference approximations are used.

More details about conditions of spatial stability necessary for long-time stable simulations are given in [12]. They are involving eigenvalues of the skew-symmetric matrix which for a lossless structure ($\mathbf{M}_{\sigma} = 0, \Omega_s = \overline{\Omega}_s$) writes as

$$\mathbf{A} = \begin{pmatrix} \mathbf{0} & -\mathbf{M}_{\mu}^{-\frac{1}{2}}\mathbf{C}\mathbf{M}_{\epsilon}^{-\frac{1}{2}} \\ \mathbf{M}_{\epsilon}^{-\frac{1}{2}}\mathbf{C}\mathbf{M}_{\mu}^{-\frac{1}{2}} & \mathbf{0} \end{pmatrix} = \begin{pmatrix} \mathbf{0} & \mathbf{A}_{21} \\ -\mathbf{A}_{21}^{T} & \mathbf{0} \end{pmatrix}. \tag{22}$$

This long-time stability is independent of the time-step. The better known second stability criterion relates to the stable time discretization. It depends on the step size and the material distribution. Thus it implies a caveat for triangular discretizations to take care of avoiding short edges in the grid(s) in order to avoid small time steps. Instead of the locally derived well-known form of the Courant-Friedrich-Levy criterion (CFL-criterion) a generalized form is derived in [12]. This form implies the eigenvalues of the iteration matrix $\mathbf{G}(\Delta t)$

$$\mathbf{G}(\Delta t) = \begin{pmatrix} \mathbf{I} & \Delta t\mathbf{A}_{21} \\ -\Delta t\mathbf{A}_{21}^{T} & \mathbf{I} + \Delta t^2\mathbf{A}_{21}^{T}\mathbf{A}_{21} \end{pmatrix}. \tag{23}$$

A stable update scheme is guarantied if all eigenvalues $\lambda_{\mathbf{G},i}$ lie within the unit circle of the complex plane while an energy conserving scheme requires that $|\lambda_{\mathbf{G},i}| = 1$ holds for the chosen time step Δt.

In [12], also the relation to the FDTD method is discussed in detail. Both methods are computationally equivalent but, until recently, only FIT allowed by its linear algebraic formulation for an easy but thorough analysis of properties like the energy conservation and for clear and elegant derivations of new developments like local subgridding [17], [18].

B. FEM with Whitney Forms and Mass Lumping

In reference [19] a leap-frog-scheme using the Galerkin approach is presented. The domain Ω_s is covered by a simplicial mesh consisting of sets of tetrahedra *T*, facets *F*, edges *E* and nodes *N*. The degree-of-freedom arrays $\boldsymbol{e}$ and $\boldsymbol{b}$ on the finite-element mesh represent electromotive forces along the edges and magnetic fluxes over the facets, respectively. They are related to the electric fluxes $\boldsymbol{d}$ and magnetomotive forces $\boldsymbol{h}$ in the dual of the FEM mesh in a one-to-one relation. The operators in the discrete constitutive laws

$$\boldsymbol{d} = \mathbf{M}^{(1)}(\epsilon)\boldsymbol{e}, \quad \boldsymbol{h} = \mathbf{M}^{(2)}(\nu)\boldsymbol{b}. \tag{24}$$

are the mass matrices which result from inner products between the Whitney basis functions (elements): With the edge elements $\boldsymbol{w}^{(1)}$ and the facet elements $\boldsymbol{w}^{(2)}$ the entries of $\mathbf{M}_{ij}^{(1)}$ and $\mathbf{M}_{ij}^{(2)}$ are given by

$$\mathbf{M}_{ij}^{(1)}(\epsilon) = \int_{\Omega_s} \epsilon\ \boldsymbol{w}_i^{(1)} \cdot \boldsymbol{w}_j^{j(1)}, \tag{25}$$

$$\mathbf{M}_{ij}^{(2)}(\nu) = \int_{\Omega_s} \nu\ \boldsymbol{w}_i^{(2)} \cdot \boldsymbol{w}_j^{(2)}. \tag{26}$$

These matrices are non-diagonal but positive-definite, symmetric and sparse.

The leap-frog-scheme for FEM with Whitney forms can then be formulated in full analogy to (20), (21):

$$\boldsymbol{b}^{k+1} = \boldsymbol{b}^{k} - \Delta t\, \mathbf{C}\boldsymbol{e}^{k+1/2}, \tag{27}$$

$$\boldsymbol{e}^{k+1/2} = \boldsymbol{e}^{k-1/2} + \Delta t \left[\mathbf{M}^{(1)}(\epsilon)^{-1}\mathbf{C}^{T}\mathbf{M}^{(2)}(\nu)\boldsymbol{b}^{k}\right]. \tag{28}$$

As in [19] it was assumed here that the current $\boldsymbol{J}$ vanishes in Ω_s. The main differences between (21) and (28) lie in the following:

1) With $\widetilde{\mathbf{C}} = \mathbf{C}^{T}$ FIT explicitly defines a curl operator on its dual grid which is applied there to $\widehat{\mathbf{h}}$ while the transpose of the curl operator $\mathbf{C}$ on the FEM grid is applied there to $\mathbf{M}^{(2)}(\nu)\boldsymbol{b}$.
2) The material operator related to the magnetic state variables is $\mathbf{M}_{\mu}$ in FIT and $\mathbf{M}^{(2)}(\nu)$ in the FEM formulation with the reluctivity $\nu = 1/\mu$.

From the physical meaning both procedures are, of course, equivalent.

As shown in [20] the first mass matrix $\mathbf{M}^{(1)}(\epsilon)$, which needs to be inverted in each time step according to (28), can be replaced by some diagonal matrix $\mathbf{H}^{(1)}(\epsilon)$ under the constraint that its entries are positive in order to provide positive-definiteness as necessary condition for the stability:

$$\mathbf{H}^{(1)}(\epsilon) = -\int_{\Omega_s} \epsilon\ \operatorname{grad} w_i^{(0)} \cdot \operatorname{grad} w_j^{(0)}. \tag{29}$$

This mass lumping gathers entries of $\mathbf{M}^{(1)}(\epsilon)$ related to edges and thus differs from summing up entries of a row as used in scalar case.

The authors of [19] state that the mass lumping procedure should be less stringent than the condition of all angles to be acute as e.g. in the classical FIT on a structured Delaunay-Voronoi grid as described above. Yet, they found out that the positiveness of the entries is not easily met in practice. Since, on the other hand, they observed that a mesh with only 5-10%

non-positive entries in $\mathbf{H}^{(1)}(\epsilon)$ is rather easily to be achieved they suggest to replace the mass matrix $\mathbf{M}^{(1)}(\epsilon)$ by a *partially* diagonalized matrix $\mathbf{H}_M^{(1)}(\epsilon)$ with as many positive entries of $\mathbf{H}^{(1)}(\epsilon)$ as possible. These percentages have to be compared with the practically found percentages of obtuse triangles in the classical FIT with structured Delaunay-Voronoi grid given e.g. in subsection III-C.

Of course, the partial mass lumping implies that no fully explicit scheme results.

The procedure for the partial diagonalization is described in detail in [19]. It is stated there that, in practice, the success of the partial diagonalization is highly dependent on the mesh generator. For the scheme without mass lumping the additional numerical effort for the iterative solution of the mass matrix equation in each time step is estimated as about 400-fold compared to a fully explicit scheme using a direct inversion of its diagonal operator. For the scheme with the partially diagonalized operator the computational load is about 400p-fold compared to the fully explicit scheme, with $0 \leq p \leq 1$ [19].

Also, one drawback of non-diagonal mass matrices compared to the classical Yee scheme (underlying the classical FIT) is pointed out in [19]: More care has to be taken in order to properly impose boundary conditions.

Allowing for some non-orthogonal regions in an orthogonal Delaunay-Voronoi grid used with classical FIT usually leads to only a small percentage of non-orthogonal cells (cf. subsection III-C). In consequence, also only a few off-diagonal entries are introduced in the corresponding material matrix. Without anticipating a systematic study of this question it seems that the effort for FIT with non-orthogonal cells and the partial mass lumping in FEM as described above is more or less comparable.

C. FEM with Orthogonal Vector Basis Functions

Several authors avoid the mass lumping because instability can not be excluded a priori, see e.g. [21], [22]. Both schemes start with the second order vector wave equation. In these two papers, a diagonal mass matrix is constructed using 2D and 3D orthogonal vector basis functions, respectively. With these basis functions a stable explicit scheme is set up. The 2D orthogonal basis presented in [21] ensures diagonality or positive-definiteness of the employed mass matrices and thus allows for a stable explicit scheme. The price for this is a blow up of the factor three in the new set of basis functions, i.e. in the degrees of freedom, but in numerical experiments the cpu time nevertheless dropped down by a factor of three for the same number of cells compared. In some numerical experiments the 3D orthogonal basis presented in [22] proved to be nearly about an order of magnitude more efficient in terms of cpu time than the traditional zeroth- and first-order vector basis [22].

D. FIT with Whitney Forms

As already noted above, in classical FIT interpolation gets necessary in the construction of the material operators on non-orthogonal grids. This destroys the one-to-one relation between the allocation of the state variables leading to off-diagonal entries in the material operators.

In search for a stable FIT scheme for non-orthogonal, non-coordinate grids an approach is studied in [23] to construct a discrete constitutive relation compatible with the integral definition of voltages and fluxes in FIT but using Whitney forms as interpolating functions.

At arbitrary points inside the cell field values are interpolated from the electric voltages $\widehat{e}_i$ using Whitney forms:

$$\boldsymbol{E}(\boldsymbol{r}) = \sum_i \widehat{e}_i \boldsymbol{w}_i^{(1)}(\boldsymbol{r}). \tag{30}$$

This is in correspondence to the FE approach with the electric grid voltage $\widehat{e}_i$ corresponding to the degree of freedom e_i.

Next, the electric flux components $\widehat{\widehat{d}}_i$ are computed according to (4) now using the interpolated field values from (30):

$$\begin{aligned} \widehat{\widehat{d}}_i &= \int_{\tilde{A}_i} \boldsymbol{D}(\boldsymbol{r}) \cdot d\boldsymbol{A} = \int_{\tilde{A}_i} \epsilon(\boldsymbol{r})\, \boldsymbol{E}(\boldsymbol{r}) \cdot d\boldsymbol{A} \\ &= \sum_j \widehat{e}_j \int_{\tilde{A}_i} \epsilon(\boldsymbol{r})\, \boldsymbol{w}_j^{(1)}(\boldsymbol{r}) \cdot d\boldsymbol{A}. \end{aligned} \tag{31}$$

Obviously the new material operator is not diagonal but it has also off-diagonal entries:

$$M_{\epsilon,ij} = \int_{\tilde{A}_i} \epsilon(\boldsymbol{r})\, \boldsymbol{w}_j^{(1)}(\boldsymbol{r}) \cdot d\boldsymbol{A} \tag{32}$$

which generally do not vanish - even for orthogonal grid duplets $(G, \widetilde{G})$.

Next, the authors of [23] investigate a single triangular cell with the barycenter as dual grid point and the dual edges intersecting the primary ones at their midpoints, i.e. the dual edges not being one straight line, but a kinked line. The resulting non-diagonal material matrix is different from the FE mass matrices. Unfortunately it is not symmetric in general.

After all, a 2D grid set up could be presented in [23] with *symmetric* material operator. This grid allows for obtuse triangles with angles up to 120°using the so-called symmetry points as dual grid points. Using these points as dual grid points the symmetry of the material operator is enforced. The symmetry point is located on the connecting line of barycenter and circumcenter of the triangle and divides this line in a 1:4 ratio. Again, this material operator is different from the one obtained by classical FIT and from the FE material operator. Thus, one important result is that "the classical FIT scheme on triangular grids ... cannot be interpreted in terms of Whitney-type basis functions." A straightforward extension of this scheme to 3D tetrahedral grids could not be found.

The new 2D algorithm was implemented and results are presented in [23]. The numerically determined convergence

rate for eigenmode computations was found to be typically between 1.3 and 2.5 depending on the grid quality and its refinement strategy.

E. *Classical FIT on Triangular Grids*

As described in subsection I-A, the angular limit to obtain an Delaunay-Voronoi grid and thus a *diagonal* material operator is 90°. Often the given geometry implies some unavoidable obtuse angles near the boundary of the meshed 2D cut of the problem domain Ω_s. If a local non-orthogonal grid is chosen in and neighbouring this triangle interpolation and projection of components becomes necessary introducing off-diagonal elements in the material operators.

Regarding the fact that these entries will only occur in a very small percentage of the matrix (cf. subsection III-C) this approach seems to be comparable to the FEM approach with mass lumping described above. Another approach could in principal follow a methodology presented in [24]. Yet, this approach based on the use of the longest-edge bisection technique introduces new points and thus destroys the topological regularity of the grid. Nevertheless both attempts or other new ideas, e.g. for FIT on an unstructured Delaunay-Voronoi diagram, to treat the problem of obtuse triangles seem to be worth some studies.

III. Examples

Several examples of simulations with URMEL-T which is based on the Finite Integration Technique on triangular grids as described above may be found in earlier publications as e.g. [3], [4], [11], [25], [8], [26], [27] or [28].

We present three typical specimen for cylindrically symmetric resonators and one waveguide example. All simulations in subsections III-A - III-C have been performed on a SUN Enterprise 450 with 300 MHz, 4 processors and 4 GB RAM.

A. *Cylindrical Resonator*

A cylindrical resonator, also denoted as 'pillbox' cavity, is suited well for convergence studies since the analytical solution is available. We chose a pillbox with the dimensions of 16.5 cm height and 22 cm width as studied in [19], see Fig. 3.

The authors of [19] computed the resonant frequencies up to 2.5 GHz with their 3D FEM code on a mesh with 7,038 tetrahedra and compared those with results from the 3D FIT code [15] with 7,293 cells using a rectangular grid with possibility of diagonal filling. Here, the eigenmodes are computed in frequency domain with the resonator option in URMEL-T for different grids. Exploiting all symmetries it is sufficient to discretize a quarter of the cavity's cross-section, an example grid with $N = 925$ points is displayed in Fig 3. As Ω equals Ω_s, the grid is nearly perfectly equilateral.

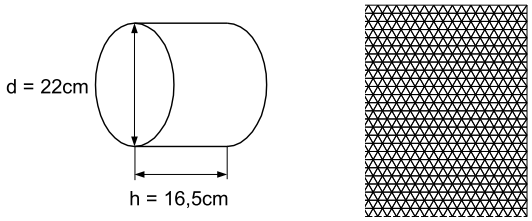

Fig. 3. Left: Cylindrical cavity, also denoted as 'pillbox' cavity. Right: Triangular grid with N = 925 grid points, i.e. 1850 triangles, for the right upper quarter of the pillbox cross-section in (r, z)-plane which only needs to be computed. In this simple case the final mesh is identical with the start mesh of the mesh generator since $\Omega = \Omega_s$ holds here.

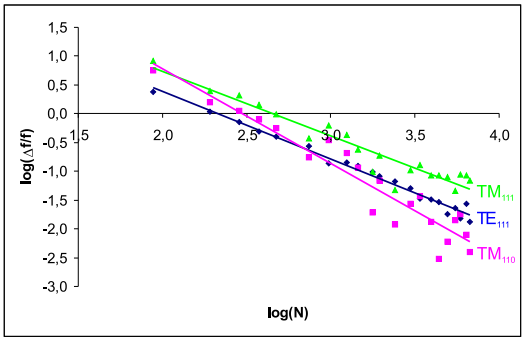

Fig. 4. Relative frequency error $\Delta f/f$ as function of number N of grid points for the TE_{111}-, TM_{110}- and TM_{111}-mode of the pillbox cavity; logarithmic scale. The convergence goes with $N^{-1.18}$ for the TE_{111}-mode, with $N^{-1.65}$ for the TM_{110}-mode and with $N^{-1.12}$ for the TM_{111}-mode.

In Fig. 4, a convergence study is presented for three selected modes. The convergence order for these modes ranges between first and second order. Best convergence is achieved for the TM_{110}-mode with $O(N^{-1.65})$. Also, the CPU time as function of the number of grid points is presented in Fig. 5. It scales with $O(N^{1.28})$. Note that three unknowns ($\widehat{e}_a$, $\widehat{e}_b$, $\widehat{e}_c$) are related to each of the N grid points.

B. *Resonator with Nose-Cone*

As another cylindrically symmetric geometry where its cross-section is neither rectangular like for the pillbox described in subsection III-A nor having a smooth and simple to approximate boundary shape like that one shown below in subsection III-C, we chose also some resonator cavity with a so-called 'nose-cone' which comes rather close to a re-entrant corner.

For comparison, an unstructured Delaunay triangulation obtained by the open source code Triangle [29] is shown in Fig. 6 together with a FIT grid of comparable number of triangles. The code Triangle generates constrained conforming Delaunay triangulations while most other codes only generate conforming, but *un*constrained triangulations. In addition to the Delaunay triangulations, Triangle also offers the related Voronoi diagram.

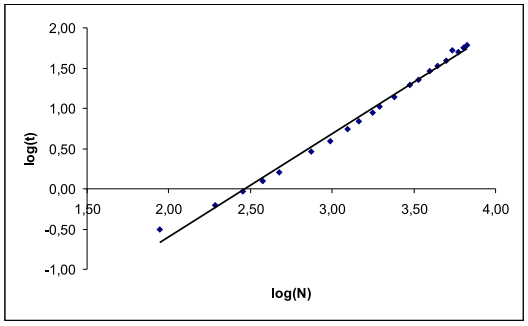

Fig. 5. CPU time t/sec as function of number N of grid points for the pillbox cavity. The cpu time depends as $t = 0.0007 \cdot N^{1.2812}$.

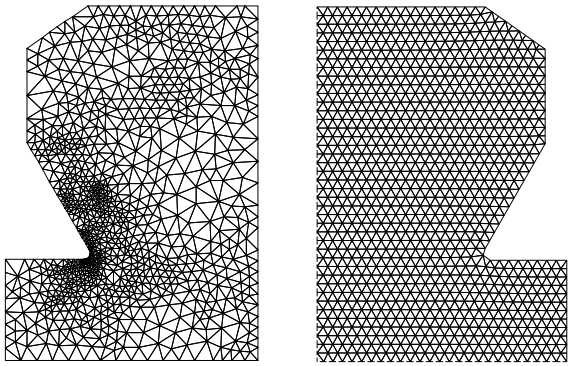

Fig. 6. Left: Delaunay triangulation with 1,860 triangles for Ω_s generated by the code Triangle [29]. Right: FIT mesh as generated for the right half of the PETRA cavity by URMEL-T with 1,015 grid points, i.e. 2,030 triangles for Ω ($\Omega \setminus \Omega_s$ is modelled as perfect conductor and thus fields are only to be computed in Ω_s). Again, for symmetry reasons only the upper left or right quarter of the cross-section in (r,z)-plane needs only to be computed.

The Triangle program informs about important grid characteristics and its construction. In the example shown in Fig. 6 the divide-and-conquer method [30] was used. In the mesh quality statistics smallest and largest area and edge are given, each. If we denote their ratio as *total* aspect ratio, the total area ratio in this example results to $2.5 \cdot 10^2$ and the total edge ratio amounts to $1.9 \cdot 10^1$. Also, the aspect ratio which relates the longest edge to the shortest altitude is given; it is 2.9374 in our example. The smallest angle is 34.004°, the largest angle is 111.5° in the grid displayed in Fig. 6. In total there are 209 obtuse triangles (11%), of those 145 (8%) have an angle between 90° and 100°, 61 (3%) an angle between 100° and 110° and 3 (0.02%) have an angle of 110° to 120°. Much more information like a list of bad and so on is available, too.

Obviously the structured FIT grid has much smaller total aspect ratios and much less obtuse triangles (cf. Table I) thanks to the equilibration algorithm imbedded in the automatic grid generation. So, the FIT grid is most regular which leads to a better condition of the matrix of the resulting linear algebraic eigenvalue problem. Also, this greater regularity has a positive impact on the maximal time step if this mesh should be used for time domain simulations. It would be interesting to compare the numerical effort necessary to reach the same error for a simulation with both type of grids, the structured Delaunay grid used in URMEL-T and the unstructured Delaunay grid. This will be the subject of a future research project.

C. *Multicell Resonators*

In the design studies for the future linear collider project TESLA [31] different multicell superconducting resonator structures have been investigated. One of them is the 4x7-cell so-called superstructure [32]. Without the attached couplers the structure is again a cylindrically symmetric one so that it can be simulated with the 2D code URMEL-T.

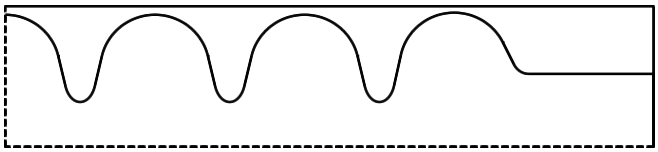

Fig. 7. Geometry of the TESLA 7-cell cavity. For symmetry reasons only the upper right quarter of the (r, z)-cross-section needs to be computed.

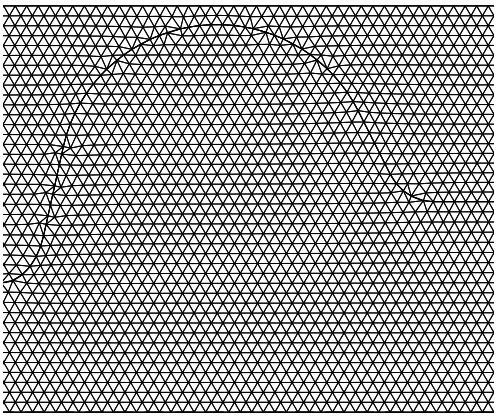

Fig. 8. Triangular grid in the right end-cell of the TESLA 7-cell cavity.

Here we chose this structure as an example to study the percentage of obtuse triangles. Fig. 7 shows the part of the cross-section used for simulation. Fig. 8 displays a zoom to the grid of the end-cell. The total number of triangles amounts to 13,366 triangles. Among them, there are 35 (0.26%) triangles with an angle larger than 90°, none of those has an angle larger than 100°.

Table I also shows the results for coarser grids used for the full 7-cell structure and a full 9-cell structure (only around 1,500 triangles per cell; 'full' refers to the complete upper half of the cross-section, 'half' to its right half as shown in Fig. 8). The percentage of obtuse triangles only amounts to 0.26% - 0.37%. Triangles with an angle larger than 100° do not always occur - if so, then they only amount to less than 0.05%. As to be expected, there seems to be a tendency that finer grids have a smaller percentage of obtuse triangles.

These far less than 1% of obtuse triangles automatically obtained in the mesh generator of URMEL-T have to be

	♯ triangles	angle $> 90°$	angle $> 100°$
9-cell, full	12,150	45 (0.37%)	4-5 (0.04%)
7-cell, full	12,320	43 (0.37%)	4-5 (0.04%)
7-cell, half	13,366	35 (0.26%)	0

TABLE I
PERCENTAGE OF OBTUSE TRIANGLES IN THE MESH OF THE TESLA 7-CELL- AND 9-CELL-RESONATOR.

compared with the 5-10% non-positive entries achieved in the partial mass lumping, e.g.. This small percentage of obtuse triangles is achieved by an equilibration procedure with low computational cost. Of course, more statistics and careful comparison of the numerical results are necessary before coming to final statements.

Fig. 9 shows some field plots for the accelerating mode in one 7-cell cavity of the 4x7-cell superstructure. The TM_{01}-mode used for the "acceleration" of electrons or positrons, respectively, passing the cavity on axis with nearly speed of light has its field maximum of the longitudinal electric field on axis such that a maximum of energy can be transferred to the particles while their passage of the structure. The plots also show that a good field flatness is achieved with the chosen cavity geometry.

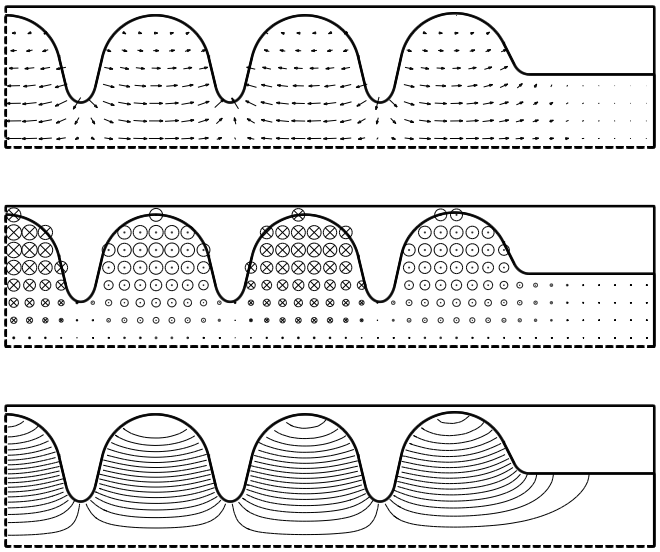

Fig. 9. Snap shots of the electric and magnetic field of the TM_{01}-mode with frequency 1.3 GHz used to accelerate electrons passing the structure on axis from left to right. The middle plot shows the azimuthal magnetic field. The size of the arrows and circles corresponds to the local magnitude of the field. Their midpoint *always* lies within Ω_s but for large magnitudes the circles or arrows might partly extend to the outside Ω_s.

D. Dielectrically Filled Rectangular Waveguide

We will show one waveguide example here, others may be found in earlier publications (see e.g. [11]). We regard the dispersion relation for a dielectric loaded waveguide. A rectangular waveguide filled with some dielectrics [4] is shown in Fig. 10.

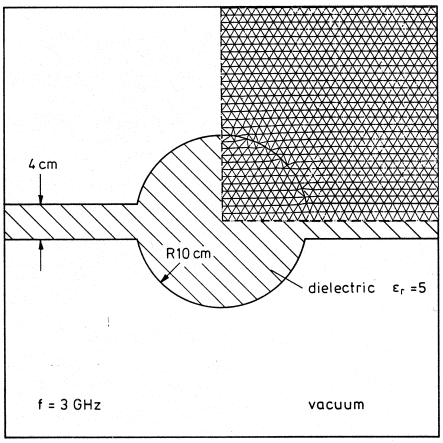

Fig. 10. Dielectric waveguide. Mesh for the computational domain.

Its fundamental mode has the frequency 3 GHz. The dispersion relation between frequency ω and propagation constant β has been computed. For different frequencies the highest β's are displayed in a fit through a few dozen distinct values in Fig. 11. Note that for each wavenumber $k_0 = \omega/c$ one URMEL–T run has to be performed.

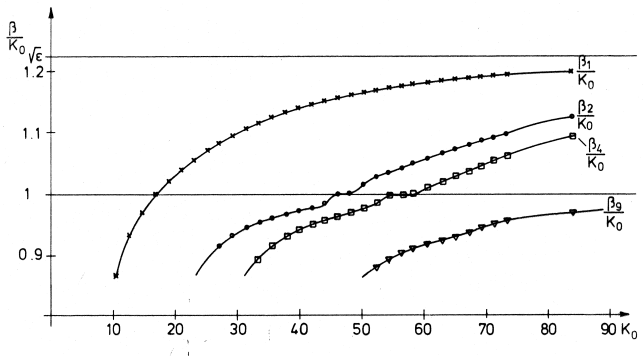

Fig. 11. Dielectric waveguide. Dispersion relation.

IV. SUMMARY

This paper revisited the application of the Finite Integration Technique on triangular grids. The corresponding code URMEL–T is successfully applied in many different locations, mainly universities and accelerator laboratories. The underlying method has been reviewed and some example resonator- and waveguide computations have been shown. Regarding the question of time domain simulations, some recent FEM approaches seeking for diagonal or partially diagonal mass matrices have been cited as well as an approach for FIT with a Whitney-based material operator.

Starting point was the following: Diagonal material operators with positive entries ensure energy conservation and stability in Yee's leap-frog-scheme for time domain simulations

(and allow for an explicit scheme). FEM with mass lumping and classical FIT on a structured Delaunay-Voronoi grid with *acute* angles both achieve a diagonal matrix with positive entries. Yet, both are not easily met in practice. Next best are positive definite symmetric material operators with only few off-diagonal entries. For FEM, a partially diagonalized mass matrix with about 5-10% non-positive entries has been suggested in literature. This has to be compared with the maximally 0.5-1% off-diagonal entries in the material matrix caused by remaining obtuse triangles in classical FIT on a structured, equilibrated Delaunay-Voronoi grid, as it was found for the examples presented here. The numerical effort to achieve a small percentage of obtuse triangles is very low - probably smaller than that one needed for the partial diagonalization of the mass matrix. Yet, this question could not be studied here but still needs more detailed studies in future.

These first studies let it seem to be worthwhile to invest some further research on a Yee-like scheme with classical FIT on structured, equilibrated Delaunay-Voronoi grids.

V. ACKNOWLEDGEMENT

The author wishes to thank R. Schuhmann and M. Dohlus for valuable hints and fruitful discussions. Also, she would like to thank H.R. Arndt for performing the simulations in subsections III-A - III-C and for his study on different open source codes for Delaunay triangulations.

REFERENCES

[1] T. Weiland, "Eine Methode zur Lösung der Maxwellschen Gleichungen für sechskomponentige Felder auf diskreter Basis," *AEÜ*, vol. 31, pp. 116–120, 1977.

[2] T. Weiland, "On the Unique Numerical Solution of Maxwellian Eigenvalue Problems in Three Dimensions," *Part.Acc.*, vol. 17, pp. 227–242, 1985.

[3] U. van Rienen and T. Weiland, "Triangular Discretization Method for the Evaluation of RF-Fields in Cylindrically Symmetric Cavities," *IEEE Transactions on Magnetics*, vol. 21, pp. 2317–2320, November 1985.

[4] U. van Rienen and T. Weiland, "Triangular Discretization Method for the Evaluation of RF-Fields in Waveguides and Cylindrically Symmetric Cavities," *Part.Acc.*, vol. 20, pp. 239–267, 1986/87.

[5] M. Clemens, R. Schuhmann, U. van Rienen, and T. Weiland, "Modern Krylov Subspace Methods in Electromagnetic Field Computation Using the Finite Integration Theory," *ACES Journal, Special Issue on Applied Mathematics: Meeting the challenges presented by Computational Electromagnetics*, vol. 11, pp. 70–84, March 1996.

[6] R. Schuhmann and T. Weiland, "Stability of FDTD Algorithm on Nonorthogonal Grids Related to the Spatial Interpolation Scheme," *IEEE-MTT*, vol. 34, pp. 2751–2754, Sept. 1998.

[7] B. Krietenstein, R. Schuhmann, P. Thoma, and T. Weiland, "The Perfect Boundary Approximation Technique Facing the Big Challenge of High Precision Field Computation," in *LINAC 98*, (Chicago, USA), pp. 695–697, 1998. http://accelconf.web.cern.ch/AccelConf/l98/PAPERS/TH4041.PDF.

[8] P. McIntosh, "RF Cavity Computer Design Codes," in *1995 Particle Accelerator Conf. (PAC'95)*, pp. 2353 – 2355, 1995. http://accelconf.web.cern.ch/AccelConf/p95/ARTICLES/MPC/MPC19.-PDF.

[9] H. Glock, K. Rothemund, and U. van Rienen, "CSC - A Procedure for Coupled S-Parameter Calculations," *IEEE Trans. on Magn.*, vol. 38, pp. 1173–1176, 2002.

[10] J.-Y. Raguin, "Network Representation of Multi-Cell Accelerating Structures," in *2001 Particle Accelerator Conf. (PAC'01)*, pp. 3027 – 3029, 2001. http://accelconf.web.cern.ch/AccelConf/p01/PAPERS/RPAH080.PDF.

[11] U. van Rienen, "Finite Integration Technique on Triangular Grids Revisited," *Int. Journal of Numerical Modelling: Electronic Networks, Devices and Fields, Special Issue "Finite Difference Time and Frequency Domain Methods"*, vol. 12, pp. 107–128, 1999. (invited paper).

[12] T. Weiland, *Computational Electromagnetics*, vol. 28 of *Lecture Notes in Computational Science and Engineering*, ch. Finite Integration Method and Discrete Electromagnetism, pp. 183–198. Springer Verlag, 2003.

[13] U. van Rienen, *Zur numerischen Berechnung zeitharmonischer elektromagnetischer Felder in offenen, zylindersymmetrischen Strukturen unter Verwendung von Mehrgitterverfahren*. PhD thesis, Darmstadt University of Technology, 1989.

[14] J. Lee, R. Lee, and A. Cangellaris, "Time-domain finite element methods," *IEEE Trans. Antennas Propagat.*, vol. 45, no. 3, pp. 430–442, 1997. (invited review paper).

[15] T. Weiland, "Time Domain Electromagnetic Field Computation with Finite Difference Methods," *Int. Journal of Numerical Modelling: Electronic Networks, Devices and Fields*, vol. 9, no. 4, pp. 295–319, 1996.

[16] K. Yee, "Numerical Solution of Initial Boundary Value Problems Involving Maxwell's Equations in Isotropic Media," *IEEE-AP*, vol. 14, pp. 302–307, 1966.

[17] P. Thoma and T. Weiland, "A Subgridding Method in Combination with the Finite Integration Technique," in *25th European Microwave Conference*, vol. 2, pp. 770 – 774, 1995.

[18] O. Podebrad, M. Clemens, and T. Weiland, "New Flexible Subgridding for the Finite Integration Technique," *IEEE Trans. Magn.*, vol. 39, pp. 1662–1665, May 2003.

[19] A. Keränen, J. Kangas, A. Ahola, and L. Kettunen, "Implicit Yee-Like Scheme on Tetrahedral Mesh," *IEEE Trans. Magn.*, vol. 38, pp. 717–720, March 2002.

[20] A. Bossavit and L. Kettunen, "Yee-like Schemes on a Tetrahedral Mesh with Diagonal Lumping," *Int. J. Numer. Modelling, Special Issue "Finite Difference Time and Frequency Domain Methods"*, vol. 12, no. 1/2, pp. 129–142, 1999.

[21] D. White, "Orthogonal basis functions for the time domain finite element solution of the vector wave equation," *IEEE Trans. Magn.*, vol. 35, no. 3, pp. 1458–1461, 1999.

[22] D. Jiao, J.-M. Jin, and E. Michielssen, "Three-Dimensional Orthogonal Vector Basis Functions for Time-Domain Finite Element Solution of Vector Wave Equation," in *Antennas and Propagation Society, 2001 IEEE Intern. Symp.*, pp. 201–207 vol.3, 2001.

[23] R. Schuhmann, P. Schmidt, and T. Weiland, "A New Whitney-Based Material Operator for the Finite-Integration Technique on Triangular Grids," *IEEE Trans. Magn.*, vol. 38, pp. 409–412, 2002.

[24] N. Hitschfeld and M. Rivara, "Non-Obtuse Boundary Delaunay Triangulations," in *6th Int. Meshing Roundtable*, (Sandia Natl. Lab., USA), p. 391, October 1997.

[25] J. Corlett and J. Byrd, "Measurement and Computation of the Higher Order Modes of the ALS 500 MHz Accelerating Cavities," in *Particle Accelerator Conf. (PAC'93)*, pp. 3408 – 3410, 1993. http://accelconf.web.cern.ch/AccelConf/p93/PDF/PAC19933408.PDF.

[26] C. Dawson, D. Dykes, and P. McIntosh, "The Tuning of the Cavity Options for DIAMOND," in *Particle Accelerator Conf. (PAC'97)*, pp. 2956 – 2958, 1997. http://accelconf.web.cern.ch/accelconf/pac97/papers/pdf/2P037.PDF.

[27] Z. Zhao, W. Pan, D. J. Sun, Y., Z. Li, H. Qu, Z. Liu, L. Feng, and K. Jin, "Design of a Copper Cavity for HLS," in *2001 Particle Accelerator Conf. (PAC'01)*, pp. 1201 – 1203, 2001. http://accelconf.web.cern.ch/AccelConf/p01/PAPERS/MPPH308.PDF.

[28] Y. Pei, W. He, K. Jin, C. Wu, and S. Dong, "The Simulation and Analysis of Secondary Emission Microwave Electron Gun," in *2nd Asian Particle Accelerator Conf. (APAC'01)*, pp. 562 – 564, 2001. http://accelconf.web.cern.ch/AccelConf/a01/PDF/WEDM02.pdf.

[29] J. R. Shewchuk, "Triangle: Engineering a 2D Quality Mesh Generator and Delaunay Triangulator," in *Applied Computational Geometry: Towards Geometric Engineering* (M. C. Lin and D. Manocha, eds.), vol. 1148 of *Lecture Notes in Computer Science*, pp. 203–222, Springer-Verlag, May 1996. From the First ACM Workshop on Applied Computational Geometry.

[30] J. Shewchuk, "Lecture Notes on Delaunay Mesh Generation," tech. rep., Departm. of Electr. Eng. and Comp. Science, University of California at Berkeley, Berkeley, CA 94720, USA, May 1999.

[31] R. Brinkmann, K. Flöttmann, J. Rossbach, P. Schmüser, N. Walker, and H. Weise, "TESLA - Technical Design Report, Part II," DESY 2001-011, Deutsches Elektronen-Synchrotron DESY, D-22607 Hamburg, Germany, March 2001. available: http://tesla.desy.de.

[32] J. Sekutowicz, M. Ferrario, and C. Tang, "Superconducting superstructure for the TESLA collider: A concept," *Phys. Rev. ST Accel. Beams*, vol. 2, no. 6, pp. 062001–1 – 062001–7, 1999. http://prst-ab.aps.org/pdf/PRSTAB/v2/i6/e062001.

Ursula van Rienen received the Diplom degree in mathematics from the Rheinische Friedrich-Wilhelms-Universität, Bonn, Germany, in 1983 and the Doctorate degree in mathematics from the Darmstadt University of Technology, Germany, in 1989. She received the *habilitation* in theoretical electrical engineering and in scientific computing in 1997.

Currently, she is a full professor at the Faculty of Engineering of Rostock University, Germany, where she was appointed to the chair of theoretical electrical engineering in 1997. She is head of a study group in computational electrodynamics. From 1983 to 1990, she was a Research Assistant at the Deutsches Elektronen Synchrotron (DESY), Hamburg, Germany. She spent several extended research stays at Los Alamos, USA, in the Accelerator Technology Division. From 1990 to 1997, she was a Research Assistant at the Darmstadt University of Technology, Germany. From 1995 to 1997 she was a Scholar of the Deutsche Forschungsgemeinschaft. The actual research covers different topics in computational electrodynamics and numerical linear algebra with practical backgrounds in accelerator physics, high voltage engineering, electromagnetic radiation, biophysics, bio- and medical technology.